Catalysis Science & Technology

ROYAL SOCIETY OF CHEMISTRY

PAPER

View Article Online
View Journal | View Issue

Cite this: *Catal. Sci. Technol.*, 2026, **16**, 2821

Co-immobilization of enzyme conjugates on monolithic hierarchical large-pore mesoporous silica for efficient cascade reactions

Georgia Mhanna, Muslim Dvoyashkin,† David Poppitz and Roger Gläser *

Received 17th December 2025,
Accepted 2nd March 2026

DOI: 10.1039/d5cy01546d

rsc.li/catalysis

Monolithic large-pore mesoporous silica (LPMS) with two hierarchically structured interconnected mesopore systems of MCM-41 (2.4–5.5 nm) and larger mesopores (20–40 nm) with high specific surface area (up to 1121 m^2 g^{-1}) and pore volume (up to 1.16 cm^3 g^{-1}) was prepared *via* partial pseudomorphic transformation. The relative fraction of the MCM-41 mesopores can be tuned from 0–1 by variation of the molar C_{18}TAOH/Br ratio as a structure-directing agent. The interconnectivity of the two mesopore systems was verified by PFG NMR diffusometry. Glucose oxidase (GOx) and horseradish peroxidase (HRP) were sequentially co-immobilized on the hierarchical LPMS materials. The co-immobilized GOx (303–350 mg g^{-1}) and HRP (95–132 mg g^{-1}) efficiently cooperate as a multi-enzyme conjugate in an activity assay oxidizing glucose to hydrogen peroxide which oxidizes 2,2′-azino-bis(3-ethylbenzothiazoline-6-sulfonic acid) diammonium salt (ABTS) to its cation. The immobilized enzymes exhibit up to 143 ± 8% of the activity of the free enzymes in solution when supported on hierarchical LPMS monoliths with particles sizes above 125 μm. Michaelis–Menten kinetics support the high enzyme activity and efficient cooperation after immobilization The enzymes are concluded to be located within the mesopores of the monoliths.

Introduction

Within each living organism, enzymes play a major role in controlling highly complex networks of chemical reactions. Essentially all metabolic pathways occur in sequential conversions denoted as cascade reactions. In nature, these pathways are efficient, specific, and optimized for particular target substrates and products.[1] Thus, multi-step enzyme-catalyzed reactions are extensively studied *in vitro* in order to transfer natural features to biotechnological applications. Particular focus is placed on artificial multi-enzyme systems for complex chemical transformations.[1–6] When more than one enzyme is to be used for a chemical conversion, consecutive conversion stages over separately supported enzyme conjugates are often applied.[7,8] However, carrying out multi-enzymatic conversions in one-pot processes is preferred due to reduction of time and costs, and lower effort for product recovery.[9–11] Several multi-enzymatic cascade reactions, *e.g.* alcohol dehydrogenase ADH-catalyzed cascades with cofactor regeneration for the synthesis of enantiomerically enriched alcohols or deracemization and stereoinversion of alcohols, might already meet industrial demands of high space–time yields and excellent product purity.[2,3]

For immobilization on solid supports, enzymes are mostly either chemically bound[12,13] or physically adsorbed[14,15] onto an insoluble, often porous support, physically trapped in a macromolecular network[16] or encapsulated within compartments.[5,17,18] Among the insoluble supports, nanoporous materials with pore widths close to the dimension of the enzymes have been intensively studied.[19–29] For instance, ordered mesoporous silica like MCM-41, MCM-48, SBA-15, and MCF were used for immobilizing several enzymes ranging from small (cytochrome c[30] or lysozyme[24,31]) to large (α-amylase[32] or cytochrome P450 (ref. 33)). Another attractive support for enzymes is large-pore mesoporous silica (LPMS).[15,34] Its large specific surface area and pore volume as well as its tunable mesoscale pores are suitable for hosting a wide range of guests, from small molecules up to large proteins.[34] Additionally, silica materials are well known for their biocompatibility, chemical inertness and modifiable surface.[19–24] Moreover, the pseudomorphic transformation of mesoporous silica can be applied for introducing a secondary pore system with a different pore width.[35–40] Pseudomorphic transformation allows obtaining monolithic materials with hierarchical pore systems exhibiting the characteristics of both a newly formed porous material, *e.g.*, MCM-41, and the

Institute of Chemical Technology, Universität Leipzig, Linnéstr. 3, 04103 Leipzig, Germany. E-mail: roger.glaeser@uni-leipzig.de; Fax: +49 341 97 36349; Tel: +49 341 97 36301

† Current address: Ruhr-Universität Bochum, Fakultät für Chemie und Biochemie, Universitätsstr. 150, D-44780 Bochum, Germany.

parent material, *i.e.*, silica beads or zeolite crystals.[34,41–44] During the transformation, the alkaline medium dissolves the silica of the parent LPMS under the influence of a structure-directing agent, *e.g.*, alkyltrimethylammonium cations (C_nTA^+). As shown for a silica gel, different pore widths of the transformation product can be achieved by using alkyltrimethylammonium cations C_nTA^+ with different alkyl chain lengths, while the degree of transformation can be controlled by the molar ratio of $C_nTAOH : C_nTABr$.[39] Additionally, the transformation leads to the formation and subsequent growth of domains containing MCM-41 homogeneously distributed over the volume of the parent silica materials.[39] However, the extent to which the resulting pore systems are interconnected, and thus the degree of hierarchical accessibility, remains poorly understood.

In this study, we report on the preparation of monolithic large-pore mesoporous silica (LPMS) with a hierarchically structured system of mesopores of two different pore widths. The first aim was to obtain these materials with different pore widths and with different fractions of the two pore systems by adjusting the conditions of pseudomorphic transformation of monolithic LPMS. Thereby, a deeper understanding of the formation mechanism of the two mesopore systems was gained by comprehensive analysis of the materials. Secondly, the hierarchically structured LPMS materials were utilized to co-immobilize two enzymes of different sizes, *i.e.*, glucose oxidase (GOx, 160 kDa, 5.5 × 7.0 × 8.0 nm (ref. 43)) and horseradish peroxidase (HRP, 44 kDa, 4.0 × 4.4 × 6.8 nm (ref. 44)), targeting the two different pore widths of the material. The activity of the supported enzyme conjugate GOx–HRP was studied with an assay requiring the concomitant action of both enzymes in a cascade reaction as an activity assay and compared to that of the free enzymes in solution and to the enzymes supported on a mesocellular foam and a silica gel. Additionally, it was a goal to confirm the hierarchy of the prepared hierarchical meso-/mesoporous LPMS materials as well as the mass-transfer properties before and after loading the materials with the two enzymes by pulsed field gradient nuclear magnetic resonance (PFG NMR). Finally, the stability of the multi-enzyme biocatalysts for reuse, towards temperature and storage conditions, was investigated.

Experimental section

Preparation of large-pore mesoporous silicas (LPMS-*x*)

LPMS materials were prepared by sol–gel synthesis combining the methods of Feng *et al.*[47] and Chen *et al.*[48] The materials were hydrothermally synthesized using tetramethyl orthosilicate (TMOS, Sigma Aldrich, 98%) as a silica source, the triblock copolymer Pluronic® F127 (Sigma Aldrich) as a structure-directing agent (SDA), dioctyl sulfosuccinate sodium salt (AOT, Sigma Aldrich, ≥97%) and *n*-butanol (VWR, ≥99%) as co-SDAs, and 1,3,5-trimethylbenzene (TMB, Sigma Aldrich, 98%) as a swelling agent. Typically, Pluronic® F127 and AOT are dissolved in a 3 mM diluted aqueous HCl solution at 318 K. Then, TMB and *n*-butanol are added with stirring to obtain a clear solution. Under continuous stirring, TMOS is added. The final molar ratio of the synthesis mixture containing TMOS : F127 : AOT : HCl : TMB : butanol was 1.0 : 0.0050 : 0.037 : 0.00032 : 0.028 : 0.39. After keeping the mixture at 318 K for 24 h, the reaction mixture was transferred into a sealed polytetrafluoroethylene (PTFE) liner (V = 50 cm^3) within a stainless steel autoclave and subjected to hydrothermal treatment at 373 K for a period of 24 h under static conditions. The solid product was collected by decantation and heated for drying and calcination at 413 K for 3 h, then 573 K for 3 h, and finally at 813 K for 5 h (heating rate of 1 K min^{-1} in all steps) in ambient air.

The LPMS material is obtained with particle sizes ≥500 μm. Different particle size fractions, *i.e.*, 35–50, 50–125, and 125–250 μm, were generated by grinding and mechanical sieving. These are denoted as LPMS-*x*, with *x* representing the maximum particle size in μm. Thus, LPMS-250 denotes the material with particle sizes in the range of 250 to 125 μm.

Preparation of hierarchical large-pore mesoporous silicas LPMS-*x*-*y*T by pseudomorphic transformation

A first series of pseudomorphic transformations were carried out to fully convert the LPMS into MCM-41-type materials using an aqueous alkyltrimethylammonium hydroxide (C_n-TAOH) solution (for the preparation, see the SI, section S1). For this purpose, 1 g of LPMS-50 material is dried at 373 K overnight, then immersed in 42 mL of the transformation (C_nTAOH) solution in a PTFE bottle (V = 250 cm^3), and hydrothermally treated for 72 h at 393 K under static conditions. The molar ratio $SiO_2 : C_nTAOH : H_2O$ in the transformation solution is 1 : 0.2 : 140. The solid transformation products are filtered off, washed with deionized water to neutral pH in the washing filtrate and calcined for 2 h at 473, 673 and 813 K with a heating rate of 10 K min^{-1} in ambient air. The resulting products are labelled according to the alkyl chain length in the C_nTAOH used, *e.g.*, C10 denotes the product of the transformation with $C_{10}TAOH$.

A second series of preparations were carried out in order to obtain partially transformed hierarchical LPMS materials with different particle sizes. For these partial pseudomorphic transformations, 1 g of dried LPMS-*x* (*cf.* above) is immersed in 42 mL of a solution consisting of different volume fractions of aqueous octadecyltrimethylammonium hydroxide ($C_{18}TAOH$) and octadecyltrimethylammonium bromide (C_{18}-TABr) solution. A constant concentration (3.36 mM) of the surfactant $C_{18}TA^+$ is applied in all the transformation solutions. The molar ratio $SiO_2 : C_{18}TA^+ : H_2O$ in the transformation mixtures amounts to 1 : 0.2 : 140. After hydrothermal treatment for 72 h at 393 K, the obtained solids are separated, washed and calcined as described for the first series of pseudomorphic transformations above. The resulting materials are denoted as LPMS-*x*-*y*T, where *x*

represents the maximum particle size and y is the volume fraction of C_{18}TAOH solution in vol%. For example, LPMS-50-33T denotes the material with a maximum particle size of 50 μm (minimum of 35 μm) after transformation with 33 vol% of C_{18}TAOH.

Characterization

The textural properties were characterized by nitrogen sorption isotherms at 77 K, using an ASAP 2010 instrument from Micromeritics®. The total specific pore volume was taken from the point at P/P_0^{-1} = 0.995. Specific surface areas and specific pore volumes for both pore systems in the hierarchical LPMS materials were determined by the *t*-plot method modified for mesoporous and hierarchical silicas within the *t*-layer region from 0.6 to 1.3 (see the SI, section S2).[8] The pore width distribution (PWD) of the fully transformed materials was obtained from the desorption branch of the nitrogen sorption isotherms using the non-local density functional theory (NLDFT) for the nitrogen–silica equilibrium transition kernel at 77 K based on a cylindrical pore model.[49] Specific BET surface areas were obtained from the linearized Brunauer–Emmett–Teller-equation in the region of relative pressure P/P_0^{-1} between 0.05 and 0.20. For partially transformed materials, the degree of (pseudomorphic) transformation was calculated by dividing the specific volume of MCM-41-type mesopores obtained from the cumulative desorption pore volume through the total pore volume at P/P_0^{-1} = 0.995. Scanning electron microscopy (SEM) images were obtained using a Leo Gemini 1530 (Zeiss) microscope at 10 kV. An in-lens secondary electron detector was used. Prior to the measurement, the samples were sputtered with gold. Phase analysis of the samples was performed by powder X-ray diffraction (XRD) using a STOE-IPDS-diffractometer (Philips X'pert Pro). The diffractograms were taken with Cu Kα radiation of 40 kV in the angle range of 2θ = 0.5–7.0° with a step size of 0.05°. Transmission electron microscopy (TEM) was performed using a JEM-2100Plus (Jeol) equipped with a LaB6 electron gun operated at an acceleration voltage of 200 kV.

The pulsed field gradient nuclear magnetic resonance (PFG NMR) spectroscopy studies were conducted using a home-built spectrometer operating at 125 MHz for protons and equipped with a pulsed magnetic field gradient unit. For diffusion experiments, the stimulated spin-echo pulse sequence was employed.[50,51] With this technique, the process of molecular propagation in the direction of the applied magnetic field gradient is monitored during the observation time t = 10 ms. Other experimentally relevant parameters were: separation between the first two 90° radio-frequency pulses τ = 1.2 ms; the duration of the gradient pulses was δ = 0.8 ms. As a diffusant, *n*-hexane (Sigma-Aldrich, 99%) was degassed by the freeze/thaw method prior to adsorption.[14] The materials under study, which were placed in NMR glass probes, were first dried for at least 6 h at 473 K and then kept in contact with the vapor of *n*-hexane overnight at 298 K at a pressure corresponding to P/P_0^{-1} = 0.9 for *n*-hexane. In this way, loading of the mesopores by gas adsorption was ensured and the amount of adsorbed *n*-hexane corresponded to a relative pore filling of ~1 in all the samples under study. Thereafter, the probes were sealed.

Enzyme immobilization

GOx (from *Aspergillus niger* 161.8 U mg^{-1}, 160 kDa purchased from Sigma Aldrich, >90%) and HRP (950–2000 U mg^{-1}, 44 kDa purchased from Sigma Aldrich, >99%) are sequentially co-immobilized on the large-pore mesoporous silicas LPMS-*x* and on the partially transformed materials LPMS-*x*-*y*T. After activation overnight under vacuum (<10 mbar) at 323 K and cooling to room temperature, 50 mg of the support material is mixed with 5.00 mL phosphate buffer solution (0.1 M, pH = 4.5, Na_2HPO_4/NaH_2PO_4 (both from Carl Roth, ≥98%)) and 5.00 mL of GOx solution (5 mg mL^{-1}) at room temperature by vortex stirring. After 48 h gentle stirring at room temperature, the GOx-containing solid is separated by centrifugation (4000 rpm for 10 min) and washed several times with phosphate buffer until no free enzyme is detected in the supernatant by UV/vis spectrometry (Avantes AvaSpec-3648; 270 nm for GOx and 403 nm for HRP, respectively). Finally, the materials are dried at room temperature for at least 6 h under vacuum (<10 mbar) and used immediately or stored at 277 K. The amount of immobilized GOx is determined by subtracting the amount in the combined supernatant washing solutions by UV/vis-spectroscopy at 270 nm from the initially added amount. Afterwards, 50 mg of the GOx-loaded LPMS-*x*-50T or LPMS-*x*-75T materials are activated overnight under vacuum (<10 mbar) at 310 K. Immobilization of HRP is performed by vortex stirring the sample with 5.00 mL phosphate buffer solution (0.1 M, pH = 5.0, Na_2HPO_4/NaH_2PO_4) and 5.00 mL of HRP solution (1.7 mg mL^{-1}) at room temperature. After 48 h of gentle stirring, the materials with the immobilized enzymes are again collected by centrifugation and washed several times with phosphate buffer until no free enzymes are detected in the supernatant. The amount of immobilized HRP is determined by subtracting the amount of HRP in the combined supernatant washing solutions from the initially added amount by UV/vis-spectroscopy at 403 nm. It was ascertained that no GOx was lost from the support during the washing steps following HRP immobilization. The resulting biocatalysts are dried as after GOx immobilization, used immediately or stored at 277 K.[52–54]

For selected supports, only GOx was immobilized. In this case, the same procedure was followed as described above, but omitting the step of HRP addition.

For comparison, a mesocellular foam (MCF) (for the preparation and characterization, see the SI, section S3) and silica-gel 62 (Sigma Aldrich, Davisil Grade 62) were included as supports for enzyme immobilization.

Activity assay

To study the catalytic activity of the enzymes, an activity assay requiring both GOx and HRP in a cascade reaction in aqueous

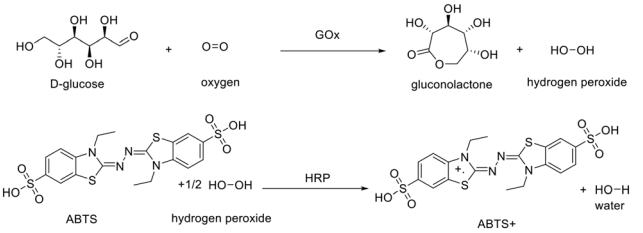

Fig. 1 Scheme of the cascade reaction from glucose and oxygen over hydrogen peroxide and the ABTS free acid to the corresponding cation $ABTS^+$ (absorption at 415 nm) catalyzed subsequently by GOx and HRP.

solution was applied (Fig. 1). In this assay, glucose and oxygen are converted to hydrogen peroxide which reacts with 2,2′-azino-bis(3-ethylbenzothiazoline-6-sulfonic acid) diammonium salt (ABTS) to its cation $ABTS^+$, the concentration of which can be quantitatively determined by UV/vis spectrometry (absorption at 415 nm).[12,52,55] In the experiments with (free) GOx and HRP in homogeneous solution or with only GOx supported, 1.00 mL of 45 mM glucose solution and 180.0 μL of a 0.4 mM solution of ABTS are mixed *via* magnetic stirring in a glass vial (V = 10 cm^3) with 200.0 μL of a GOx solution (0.6 mg mL^{-1}) or 200.0 μL of a suspension of the supported GOx (containing 0.6 mg mL^{-1} GOx), and 1.80 mL of phosphate buffer solution (0.1 M, pH = 7.0, Na_2HPO_4/NaH_2PO_4). Then, 200.0 μL of an HRP solution (0.2 mg mL^{-1}) is added. The mass ratio of HRP : GOx in all cases is 1 : 3 and the molar ratio is 1 : 1, respectively. For the co-immobilized GOx and HRP, the mass of the dried biocatalyst particles is chosen to keep the same enzyme amount as for the free enzymes in the reaction mixture based on the determined amount of immobilized GOx and HRP. The dried biocatalyst particles with both supported enzymes are directly added to the same mixture of glucose and ABTS solution as for the free enzymes, while 2.20 mL of phosphate buffer solution is added.

The resulting reaction mixture is then left stirring at room temperature for 5 min. The reaction progress is monitored following the absorption of the cation $ABTS^+$ at 415 nm by UV/vis-spectrometry (Avantes AvaSpec-3648).[12,52,55] The catalytic activity is determined as the average reaction rate using the concentration change of $ABTS^+$ over time from 0 to 10 min, with t = 0 marking the start of the reaction when HRP solution is added. The relative activity RA is then calculated as the ratio of the average reaction rate for the immobilized enzymes and the average reaction rate for the free enzymes in solution under the same reaction conditions. The normalized activity NA is obtained by normalizing the average reaction rate for the immobilized enzymes and the free enzymes to the concentration of the enzymes in the reaction medium (eqn (1)).[54,56]

$$\mathrm{NA} = \mathrm{RA} \cdot \frac{c_{\text{free enzymes}}}{c_{\text{immobilized enzymes}}} \quad (1)$$

The reusability of selected immobilized biocatalysts was studied by washing the supported enzymes three times with 10 mL phosphate buffer solution and repeating the activity assay twice. Furthermore, the thermal stability of both free and immobilized enzymes towards denaturation was studied by carrying out the activity assay after different incubation times (24, 48, 72, 100, 120, 140, or 160 h) at 278 K and after an incubation time of 4 h at different temperatures (278, 288, 298, 308, 318, 333, or 343 K).

To determine the Michaelis–Menten constants for the free and immobilized GOx and HRP, the activity assay is conducted with a 5-fold batch with respect to the one reported above. 5.0 mL of glucose solution (0, 5, 15, 25, 45, 90, or 120 mM) and 0.9 mL of ABTS solution (0.4 mM) are mixed with 1.0 mL of free GOx (0.6 mg mL^{-1}) or 1.0 mL of the suspension (containing 0.6 mg mL^{-1} immobilized GOx), and 9.0 mL of phosphate buffer solution (pH = 7) and 1.0 mL of HRP solution (0.2 mg mL^{-1}) are added marking the start of the reaction, *i.e.*, t = 0. The substrate concentration c_S is obtained from the concentration of $ABTS^+$ assuming stoichiometric conversion according to Fig. 1.[12,52] The initial reaction rate r_0 is calculated from the slope of dependence of c_S on time at t = 0, assuming that the HRP catalysed step is non-limiting and the cascade operates in a regime where $ABTS^+$ formation is strictly proportional to GOx turnover. Thereafter, the Lineweaver–Burk plot, *i.e.*, the double reciprocal plot of r_0^{-1} *vs.* c_S^{-1}, is generated from which the apparent rate r_{max} and the apparent Michaelis–Menten constant K_M are extracted (see the SI, section S5). Additionally, the catalytic reaction rate constant k_{cat} (eqn (2)) and the catalytic efficiency $k_{cat}\ K_M^{-1}$ are estimated, respectively, where c_E represents the enzyme concentration in the reaction mixture.

$$k_{cat} = \frac{r_{max}}{c_E} \quad (2)$$

Moreover, the activity assay using the same batch size as for the determination of the Michaelis–Menten constant is conducted at different temperatures in the range of 288 to 328 K, in order to determine the influence of the temperature increase on the enzyme activities.

Results and discussion

Large-pore mesoporous silica (LPMS)

As a starting material for the hierarchical materials, large-pore mesoporous silica (LPMS) was prepared. The nitrogen sorption isotherm and the pore width distribution of the resulting material are shown in Fig. 2. The LPMS has a high specific pore volume (1.76 $cm^3\ g^{-1}$), a high specific surface area (324 $m^2\ g^{-1}$) and pore width distribution with a maximum D_p = 35 nm.

Most importantly, the LPMS material is obtained as monolithic particles with sizes ≥500 μm. This makes it an attractive support for continuous processes as opposed to many other mesoporous materials which are typically obtained as powders.

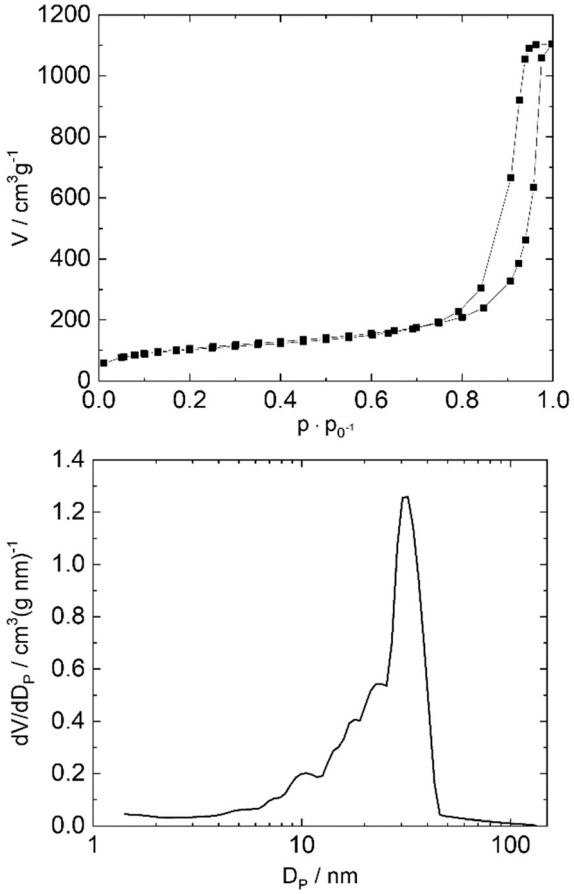

Fig. 2 Nitrogen sorption isotherm (top) and pore width distribution (bottom) from the desorption branch (Broekhof–DeBoer) for LPMS.

Hierarchical large-pore mesoporous silica LPMS by pseudomorphic transformation

An additional system of ordered mesopores typical for MCM-41-type materials was introduced into the LPMS by a post-synthetic pseudomorphic transformation.

In a first series of transformations, the alkyl chain length *n* of the surfactant C_nTAOH as a structure-directing agent was varied between 10 and 22 carbon atoms while completely converting the LPMS to an MCM-41-type material. The formation of the ordered mesopore system of MCM-41 is confirmed by the XRD patterns shown for the LPMS after transformation with $C_{18}TAOH$ (C18, Fig. 3). The major reflection at 2θ = 2.1° corresponds to MCM-41 pores related to the 100 plane. Upon increasing the alkyl chain length in the structure-directing agent from 10 to 22 carbon atoms, the specific pore volume and the pore width of the transformation products increase from 0.42–1.16 $cm^3\ g^{-1}$ and from 2.4–5.5 nm, respectively (Fig. 4 and Table 1). The nitrogen sorption isotherms (Fig. 4, top) also confirm the increase in the specific surface area from 558–1121 $m^2\ g^{-1}$ with increasing alkyl chain length of C_nTAOH (*cf.* Table 1). The only exception is sample C22 for which a lower specific surface area and a broader pore width distribution are observed, presumably due to an incomplete transformation

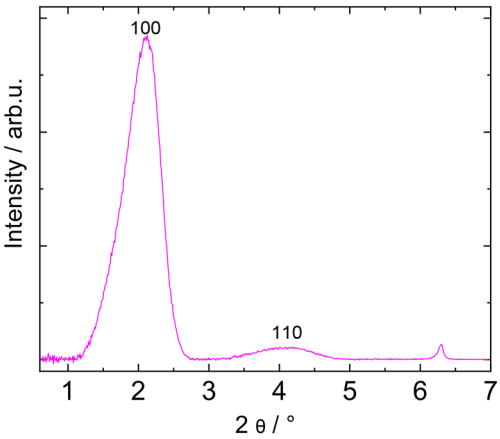

Fig. 3 Exemplary small angle XRD pattern for the completely transformed material C18.

into MCM-41 (see the SI, section S2 and Fig. S2 for the nitrogen sorption isotherm of sample C22).

A second series of pseudomorphic transformations were carried out to obtain large-pore mesoporous silica with a

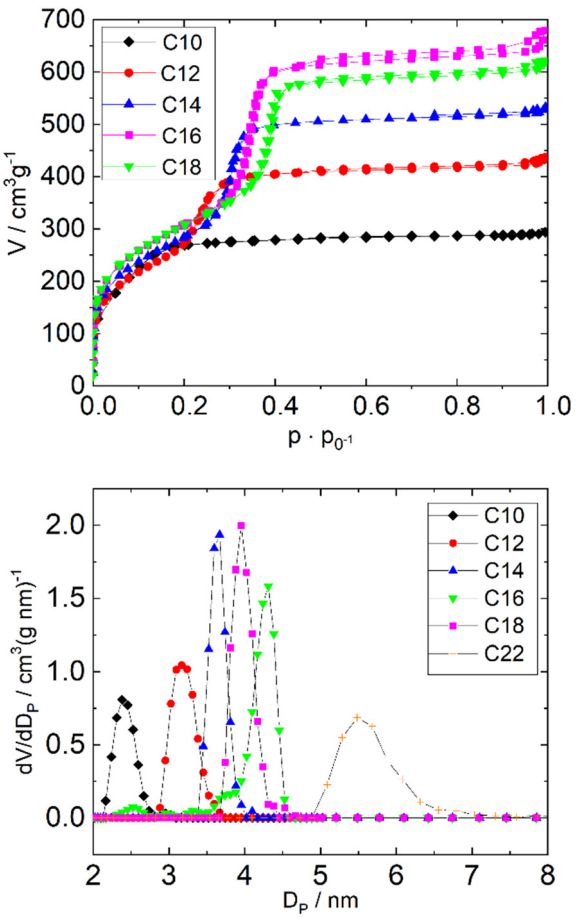

Fig. 4 Nitrogen sorption isotherms (top) and pore width distributions from the desorption branch of the isotherms (NLDFT) (bottom) for LPMS materials after pseudomorphic transformation in the presence of surfactants with different alkyl chain lengths *n* of C_nTAOH.

Table 1 Specific pore volume $V_{P(BJH\ des.)}$, specific surface area $A_{(BET)}$, and maximum pore width $D_{p(NLDFT)}$ of LPMS materials after pseudomorphic transformation in the presence of surfactants with different alkyl chain lengths *n* of C_nTAOH

Material	$V_{P(BJH\ des.)}$/cm^3 g^{-1}	$A_{(BET)}$/m^2 g^{-1}	$D_{p(NLDFT)}$/nm
C10	0.42	923	2.4
C12	0.65	966	3.2
C14	0.96	1039	3.6
C16	1.16	1121	4.0
C18	1.09	1100	4.2
C22	1.10	558	5.5

hierarchical bimodal pore system. For these transformations, both C_{18}TABr and C_{18}TAOH were used in different ratios to control the degree of transformation. The partial transformation of LPMS is graphically illustrated in Fig. 5.

The nitrogen sorption isotherms and the pore width distributions of the partial transformation products of the LPMS with a particle size of 50 μm (LPMS-50) are shown in Fig. 6. With increasing volume fraction of C_{18}TAOH solution from 0 up to 100% in the transformation mixture, the pore volume of MCM-41 pores increases and that of LPMS pores decreases. This corresponds to an increasing transformation degree from LPMS to MCM-41. While the average pore width of the LPMS-pores slightly decreases with increasing transformation degree, the width of MCM-41 pores remains constant (Fig. 6, bottom).

By means of small angle XRD patterns, the transformation of the mesopore system can be seen. With the exception of the LPMS-50 parent material where no peak can be detected, likely due to the detection limit, diffraction peaks appear with increasing volume fraction of C_{18}TAOH solution (Fig. 7). Thereby, the peaks are shifted to higher diffraction angles with increasing volume fraction of C_{18}TAOH solution indicating the formation of smaller mesopores.

For determining the specific pore volume of MCM-41 pores and that of LPMS pores separately, the cumulative pore volume of the material determined by the *t*-plot method from the nitrogen sorption isotherms was considered. As shown in Fig. 8 (bottom), the first decrease in cumulative pore volume was attributed to the MCM-41 pores with small widths between 0 and 5 nm and the second decrease to the LPMS pores with larger widths between 20 and 40 nm. The same procedure was followed to determine the specific surface area

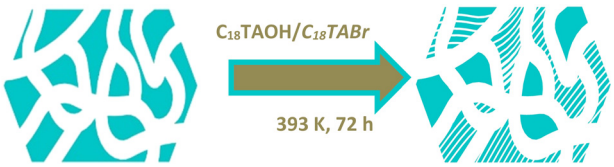

Fig. 5 Schematic illustration of the partial pseudomorphic transformation of LPMS materials into hierarchical bimodal LPMS-*x*-*y*T by using a mixture of C_{18}TABr and C_{18}TAOH in the transformation mixture.

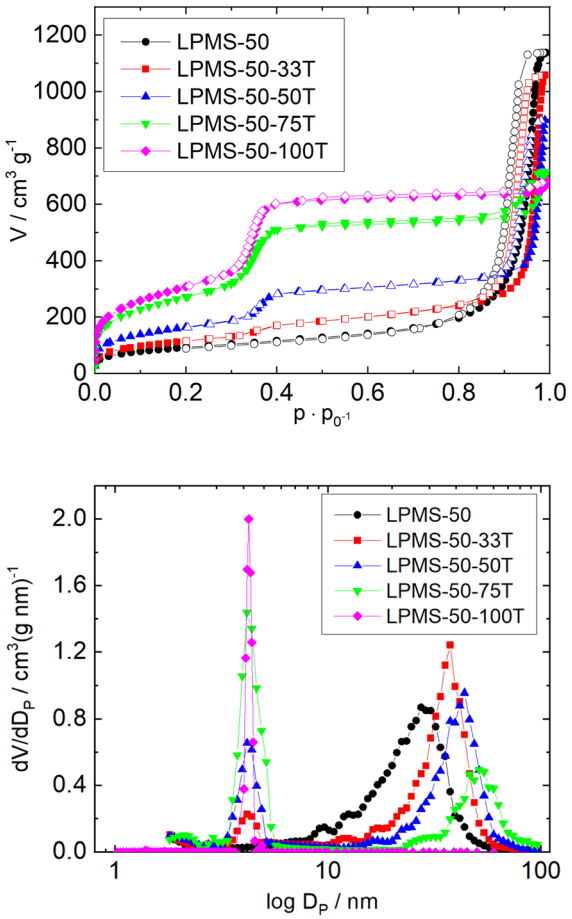

Fig. 6 Nitrogen sorption isotherms (top) and pore width distributions (bottom) from the desorption branch of the isotherms (NLDFT) for LPMS-50-*y*T materials after partial pseudomorphic transformation in the presence of different fractions of C_{18}TAOH relative to C_{18}TABr.

of the MCM-41 and LPMS pores separately (Fig. 8, top). Table 2 summarizes the values for all LPMS-50-*y*T materials

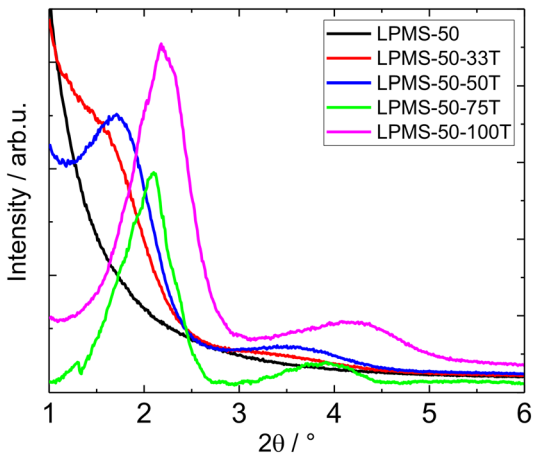

Fig. 7 Small angle XRD patterns for the completely transformed material C18 for LPMS-50-*y*T materials after partial pseudomorphic transformation in the presence of different fractions of C_{18}TAOH relative to C_{18}TABr.

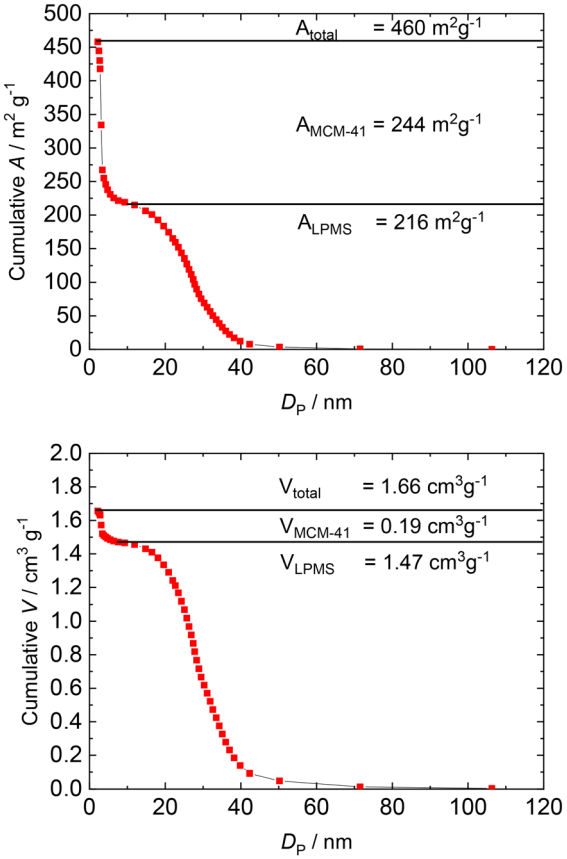

Fig. 8 Cumulative specific surface area A (top) and cumulative specific pore volume V (bottom) as a function of pore width D_P obtained by nitrogen sorption at 77 K (t-plot method) for determination of the contributions of LPMS and MCM-41 to the overall values (shown for the partially transformed large-pore mesoporous silica LPMS-50-33T).

with bimodal pore systems including the calculated volume fraction of MCM-41 in the total pore volume.

Evidently, the fraction of MCM-41 pores X_{MCM-41} increases with increasing fraction of C_{18}TAOH solution. However, it does not directly correlate to the volume fraction of C_{18}TAOH solution in the transformation mixture. For instance, in LPMS-50-50T obtained from 50 vol% of C_{18}TAOH solution, only a fraction of 0.25 of the total specific pore volume is contributed by MCM-41 pores.

SEM images show no alteration of particle size or geometry after pseudomorphic transformation. High resolution SEM

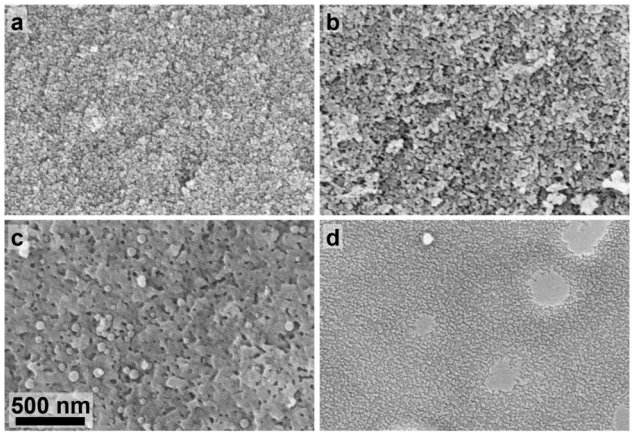

Fig. 9 SEM images of the large-pore mesoporous silica LPMS-50 (a), and the hierarchical large-pore mesoporous silica from partial pseudomorphic transformation LPMS-50-50T (b), LPMS-50-75T (c), and LPMS-50-100T (d).

images of the particle surfaces show a contradictory effect compared to results from nitrogen sorption and small angle XRD. Whereas the LPMS-50 material show very small pore widths close to the resolution limit, the pore width seems to increase towards 75% volume fraction of C_{18}TAOH (Fig. 9). Surprisingly, LPMS-50-100T shows a very smooth surface where only small pores can be observed.

TEM imaging shows the homogeneous distribution of large mesopores which are unordered for the material LPMS-50. With adding C_{18}TAOH, these large pores become even larger until they disappear for the LPMS-50-100T material (Fig. 10). These results correlate with those from nitrogen sorption and observations in SEM imaging indicating a consumption of the LPMS material during pseudomorphic transformation. Additionally, the formation of small mesopores in the skeleton of the large mesopores can be observed in all materials with added C_{18}-TAOH. These small mesopores, having pore distances of about 4 nm, are homogeneously distributed and show an unordered pore structure as well. The fraction of the small mesopores increases with increasing volume fraction of C_{18}TAOH as was found by nitrogen sorption (see Fig. 6).

Co-immobilization of GOx and HRP

To evaluate the applicability of hierarchical LPMS materials for immobilization of multi-enzyme conjugates, glucose

Table 2 Specific pore volume and specific surface area for the MCM-41 and LPMS pores as well as the calculated volume fraction of MCM-41 pores X_{MCM-41} in the initial LPMS and the pseudomorphically transformed LPMS-50-yT materials

Material	V_{MCM-41}/cm³ g⁻¹	V_{LPMS}/cm³ g⁻¹	X_{MCM-41}	A_{MCM-41}/m² g⁻¹	A_{LPMS}/m² g⁻¹
LPMS-50	n.a.[a]	1.54	n.a.[a]	n.a.[a]	412
LPMS-50-33T	0.19	1.47	0.11	244	216
LPMS-50-50T	0.37	1.10	0.25	500	180
LPMS-50-75T	0.70	0.75	0.48	950	100
LPMS-50-100T	0.95	0.11	0.90	1094	28

[a] n.a.: not applicable.

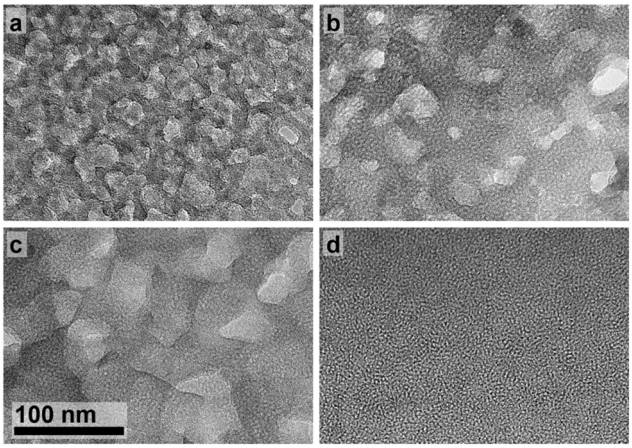

Fig. 10 TEM images of the large-pore mesoporous silica LPMS-50 (a), and the hierarchical large-pore mesoporous silica from partial pseudomorphic transformation LPMS-50-50T (b), LPMS-50-75T (c), and LPMS-50-100T (d) showing the presence of small mesopores.

oxidase (GOx) and horseradish peroxidase (HRP) were used as model enzymes. First, loadings of each enzyme on LPMS materials for different starting concentrations of enzymes were determined (see the SI, section S4 and Fig. S4–S6). Based on these results, loadings of the enzymes were chosen for the co-immobilization of both GOx and HRP by sequential adsorption. The general concept is graphically illustrated in Fig. 11. Since GOx has dimensions of 5.5 × 7.0 × 8.0 nm,[45] it is assumed to fit into the large pores of the parent LPMS, but excluded from the small MCM-41 pores. These can, however, accommodate HRP (dimensions of 4.0 × 4.4 × 6.8 nm (ref. 46)).

As a first test, whether GOx can fit into the large pores of LPMS and HRP into the small pores of MCM-41, the effect of the enzyme loading on the specific pore volume before and after immobilization was studied. Thus, GOx was immobilized on the parent LPMS-50 and HRP on the completely transformed material LPMS-50-100T with a maximum particle size of 50 µm. Upon loading with the enzymes, the specific pore volume decreases from 1.54 to 1.31 $cm^3\ g^{-1}$ for LPMS-50 + GOx and from 1.06 to 0.84 $cm^3\ g^{-1}$ for LPMS-50-100T + HRP. This is an indication that the enzymes occupy the pore spaces rather than being located on the outer surface of the materials. However, a partial pore blocking effect cannot be excluded.

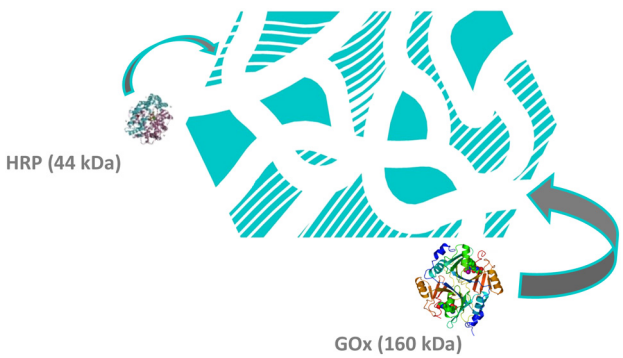

Fig. 11 Schematic illustration of the co-immobilization of GOx and HRP within the small and large pores of the LPMS-*x*-*y*T support.

The adsorption of GOx was conducted first followed by the adsorption of HRP. It is assumed that after filling the larger pores with the GOx enzymes, the smaller pores (and potentially space in the larger pores not occupied by GOx) can be loaded with the HRP enzymes. To avoid leaching of GOx during sorption of HRP, a higher pH of the buffer solution during the immobilization of HRP was applied (see the Experimental section). However, minor leaching of the already adsorbed GOx enzymes occurs. This can be monitored by UV/vis-spectroscopy and the final loading of GOx recalculated considering the loss due to leaching.

As stated in the literature, an HRP : GOx mass ratio of 1 : 3 was required for a maximum overall activity for the chosen model reaction (*vide infra*).[52–55] Thus, the loading ratios were adjusted accordingly. The obtained HRP and GOx loadings by sequential co-immobilization on various materials required for the first investigation are summarized in Table 3. It shows that the targeted ratio of the enzyme loadings was achieved and that the overall loadings of GOx and HRP are in a comparable range, except for the completely transformed material LPMS-50-100T + GOx/HRP with a considerably lower loading of both enzymes. This could be due to the presence of only smaller pores within the LPMS-50-100T material, where accessibility into the inner pores could be hindered and pore blocking is more likely.

Hierarchy of the bimodal pore system and enzyme loading probed by PFG NMR

Diffusometry by PFG NMR was applied to gain further insight into the connectivity of the two mesopore systems in partially transformed large-pore mesoporous silica and into the location of the co-immobilized enzymes GOx and HRP. The measured echo attenuations from the PFG NMR spectroscopy with *n*-hexane as a diffusant are shown in Fig. 12. The curves show a pronounced non-monoexponential decay suggesting the presence of more than one diffusion coefficient, which might result from the different diffusion regimes of *n*-hexane. According to the sample preparation procedure, it is possible that

Table 3 Loading of GOx and HRP after sequential co-immobilization on the partially transformed large-pore mesoporous silica LPMS-50-*y*T, a mesocellular foam MCF and silica-gel 62

Material	HRP loading/mg g^{-1}	GOx loading/mg g^{-1}
LPMS-50 + GOx/HRP	112	303
LPMS-50-33T + GOx/HRP	95	285
LPMS-50-50T + GOx/HRP	128	350
LPMS-50-75T + GOx/HRP	132	346
LPMS-50-100T + GOx/HRP	34	86
MCF + GOx/HRP	145	374
Silica-gel 62 + GOx/HRP	131	371

n-hexane molecules diffuse not only within the pores of the materials, but also partially through the gas phase between the particles. In that case, known as the long-range diffusion,[57] the resulting diffusivity might be even higher than that of the bulk liquid *n*-hexane. Thus, for obtaining the intraparticle diffusion coefficients $D_{experimental}$, only the slowest decays in the range of high-gradients were analyzed. The corresponding fittings are represented by solid lines in Fig. 12. The results of such fitting are summarized by the values of $D_{experimental}$ in Table 4. The root mean square displacement (RMSD) for each measured intraparticle diffusivity was calculated using the Einstein equation (eqn (3)):

$$\mathrm{RMSD} = \sqrt{6 \cdot t \cdot D_{experimental}} \quad (3)$$

where t is the observation time. The corresponding calculated values are reported in Table 4.

According to the textural data obtained for the materials under study, the fraction of smaller mesopores, *i.e.*, of the MCM-41-type, increases for higher degrees of transformation (see Table 2). Consistently, it is observed that the self-diffusion coefficient of *n*-hexane monotonically decreases. If transformation occurs homogeneously on the length scale of probed RMSDs (~5–10 μm), and there are no significant diffusion barriers on the interface of larger and smaller mesopores, the observed diffusivities for the intermediate degrees of transformation under conditions of fast diffusion exchange between smaller and larger mesopores can be predicted, if those values for the parent and completely transformed materials are known. These expected diffusion coefficients $D_{expected}$ of each LPMS material partially transformed into MCM-41 are then calculated using eqn (4):

$$D_{expected} = \frac{V_{LPMS}}{V_{total}} \cdot D_{LPMS} + \frac{V_{MCM\text{-}41}}{V_{total}} \cdot D_{MCM\text{-}41} \quad (4)$$

where V_{LPMS}, $V_{MCM\text{-}41}$, and V_{total} correspond to the specific pore volumes of LPMS and MCM-41 and specific total pore volume, respectively, extracted from the nitrogen sorption data presented in Table 2. Assuming equal densities of *n*-hexane in the larger and smaller mesopores, the fraction of molecules having diffusivities of D_{LPMS} and $D_{MCM\text{-}41}$ can be represented as V_{LPMS}/V_{total} and $V_{MCM\text{-}41}/V_{total}$, respectively. Since no data were found in the literature on previous PFG NMR conducted for LPMS materials, D_{LPMS} was taken as the experimental value of the diffusion coefficient of pure LPMS (1.40×10^{-09} m^2 s^{-1}), whereas $D_{MCM\text{-}41}$ corresponds to the estimated value obtained by extrapolation of the diffusion coefficients when the volume fraction of MCM-41 is equal to one. It is worth noting that this value (3.75×10^{-10} m^2 s^{-1}) is in agreement with the literature diffusion coefficients of *n*-hexane in materials fully transformed into MCM-41 by pseudomorphic transformation.[58] The calculated values of $D_{expected}$ for the different LPMS materials used in this report are summarized in Table 4.

Concerning the LPMS materials loaded with both GOx and HRP, the spin-echo attenuation curves in Fig. 12 (bottom) were similarly obtained and $D_{experimental+GOx/HRP}$ was extracted from the slower components of these curves and presented in Table 4.

Fig. 13 presents the variation in diffusion coefficients in terms of $X_{MCM\text{-}41}$, which corresponds to the MCM-41 volume fraction calculated from the nitrogen sorption data (Table 2). $D_{expected}$ was also plotted as a reference value for the experimental ones. As shown in Fig. 13, the experimental values of diffusivities for the material without enzymes are comparable to the $D_{expected}$, except for the material LPMS-75T that shows a lower diffusion rate of *n*-hexane. This is an indication of a higher interconnectivity of the two mesopore systems for this high degree of transformation. For the materials loaded with enzymes, the decrease of the diffusion coefficients within the intraparticle volume is an indication that the enzymes occupy the pore space and are not located on the outer surface of the materials. In addition, when comparing the materials with and without enzymes, a rather minor reduction of diffusivities (30–40%) can be an indication that the enzymes do not block the pores.

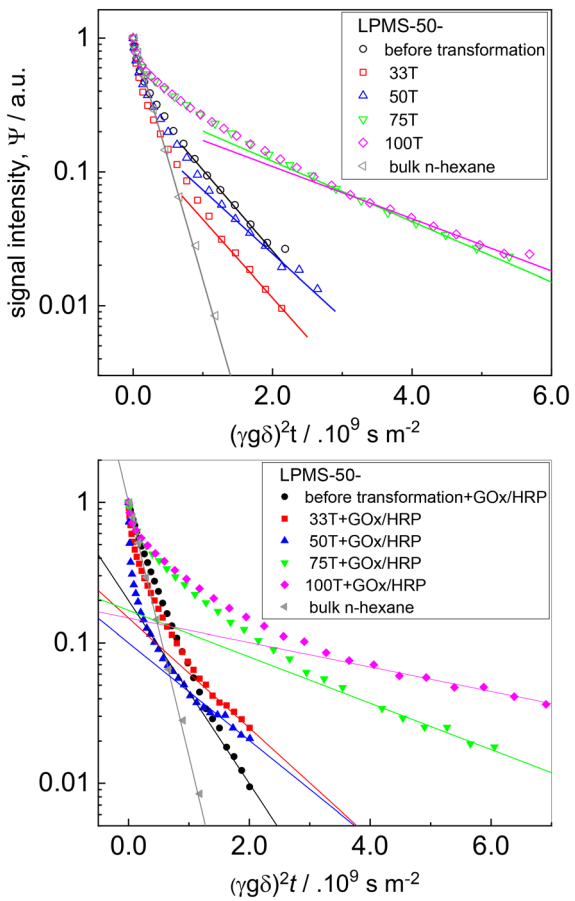

Fig. 12 Spin-echo diffusion attenuation curves for *n*-hexane in LPMS-50 and the partially transformed, hierarchical large-pore mesoporous silicas LPMS-50-*y*T before (top) and after loading with both GOx and HRP by co-immobilization (bottom).

Table 4 Calculated (expected) and experimentally determined diffusion coefficients $D_{expected}$ and $D_{experimental}$ as well as the root mean square displacement RMSD at 298 K for the large-pore mesoporous silicas LPMS-50-*y*T before and after co-immobilization with GOx and HRP

Material	$D_{expected}$/m^2 s^{-1}	$D_{experimental}$/m^2 s^{-1}	RMSD/μm	$D_{experimental+GOx/HRP}$/m^2 s^{-1}	$RMSD_{+GOx/HRP}$/μm
LPMS-50	1.40×10^{-09}	1.40×10^{-09}	9.2	1.5×10^{-09}	9.5
LPMS-50-33T	1.31×10^{-09}	1.35×10^{-09}	9.0	9.0×10^{-10}	7.3
LPMS-50-50T	1.14×10^{-09}	1.10×10^{-09}	8.1	8.0×10^{-10}	6.9
LPMS-50-75T	9.05×10^{-10}	5.20×10^{-10}	5.6	3.8×10^{-10}	4.8
LPMS-50-100T	4.81×10^{-10}	4.50×10^{-10}	5.2	2.0×10^{-10}	3.5
Bulk *n*-hexane	n.a.[a]	4.18×10^{-09}	n.a.[a]	n.a.[a]	n.a.[a]

[a] n.a.: not applicable.

As a conclusion, according to the PFG NMR findings, a fast exchange between larger and smaller mesopores has been observed on the length scale of ~5–10 μm, suggesting a hierarchal nature and an interconnectivity of the two mesopores in all LPMS-*y*T materials obtained by pseudomorphic transformation.

Catalytic activity of the immobilized enzyme conjugate

Fig. 14 summarizes the normalized overall activity of the enzymes immobilized on hierarchical LPMS-50-*y*T materials as well as on a mesocellular foam (MCF) and a silica gel for comparison. The co-immobilized GOx and HRP are less active by 28–33% than the free enzymes in solution, taken as 100% of the normalized activity. Interestingly, the different transformation degrees of the LPMS supports, *i.e.*, LPMS-50-50T or LPMS-50-75T, have essentially no influence on the activity. However, the enzymes immobilized on the hierarchical, monolithic LPMS materials are significantly more active than those on the mesocellular foam or the silica gel as a support (Fig. 14). This might be related to the more efficient interaction of the two enzymes when supported in the pores of the hierarchical LPMS materials. As an additional notice, all the investigations were conducted with a negative control, *i.e.*, in the presence of the materials without the supported enzymes, and 0% normalized activity has been recorded.

As Fig. 14 also shows, the activity of the enzymes co-immobilized on LPMS-50-50T and LPMS-50-75T decreases considerably when used again for two cycles. This activity loss is consistent with several literature studies, reporting activity losses of GOx immobilized on mesoporous silica in the range of 10–20% in each cycle.[59,60] However, despite the lower activities compared to that of LPMS-based biocatalysts for the fresh materials, the enzymes supported on MCF and silica-gel 62 undergo a less radical decrease in the activities in the first and second reuse. The reason for the lower activities of the MCF- and silica gel-based catalysts could be due to the smaller pore widths of the two supports (with a 22 nm cage width and a 17 nm pore window width for MCF and a 15 nm pore width for silica-gel 62), resulting in a lower pore filling, especially with the larger GOx enzymes. The smaller pores and pore openings could, however, protect the supported enzymes more effectively

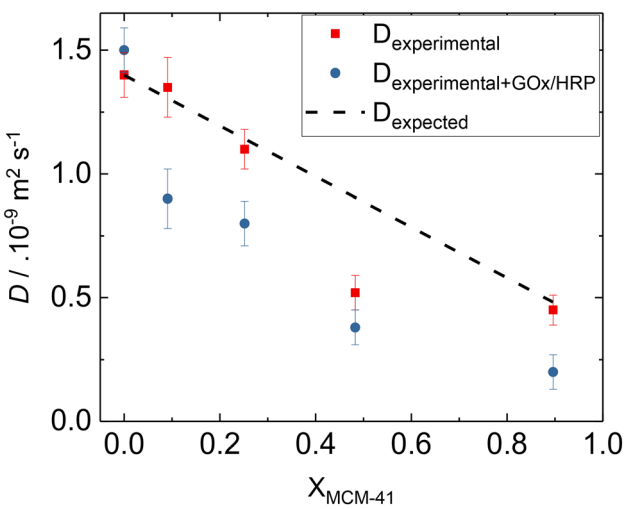

Fig. 13 $D_{experimental}$ for the large-pore mesoporous silicas LPMS-50-*y*T before and after co-immobilization with GOx and HRP as a function of volume fraction of MCM-41 pores (X_{MCM-41}, *cf.* Table 2). $D_{expected}$ denotes the values of the diffusion coefficients calculated from eqn (4).

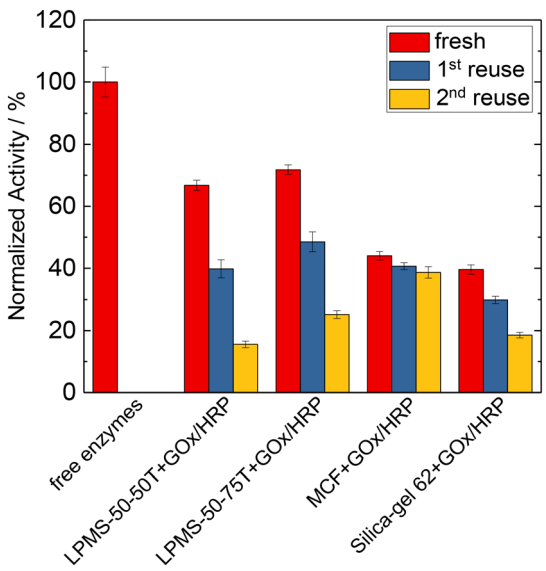

Fig. 14 Normalized activity of the free enzymes GOx and HRP and of co-immobilized GOx and HRP on large-pore mesoporous silica with different MCM-41 pore fractions LPMS-50-*y*T, a mesocellular foam MCF and silica-gel 62. Besides the values for the fresh catalysts, the ones for the first and second reuse are also shown.

towards leaching and lead to a lower activity decrease upon the first and second reuse. Similar cases of enzyme protection against activity loss when immobilized in small pores were reported in the literature.[14,60–62]

Michaelis–Menten investigations for free and immobilized GOx and HRP

In order to confirm the impact of the transformation degree of the hierarchical LPMS materials on the catalytic properties of the supported enzymes, Michaelis–Menten investigations were conducted. In addition, an insight into the variation of the catalytic properties of GOx in solution, individually immobilized, or co-immobilized with HRP should be gained. Therefore, the activities of GOx immobilized on LPMS-50-50T and LPMS-50-75T, either alone or with HRP, were recorded and compared to the ones of the free GOx in solution. The apparent Michaelis–Menten constant K_M and maximum reaction rate r_{max} were determined for the free GOx in solution as well as for each material by fitting the initial reaction rate data to the Lineweaver–Burk diagram (see the SI, section S4 and Fig. S10). To ensure a plausible comparative analysis with the benchmark studies,[52,63,64] the same mathematical framework using the Lineweaver–Burk fitting was used, although this linear fitting may disproportionately weight experimental errors at low substrate concentrations.

The calculated apparent K_M for free GOx in solution (1.45 mM) is lower by a factor of 2–29 than the ones reported in the literature for similar reaction conditions (2.6–41.8 mM).[52,63,64] This can indicate inhibition of the GOx activity under the selected reaction conditions. It is known that the activity of GOx can be reduced when H_2O_2 accumulates around the active sites.[65] Due to the high substrate concentrations used in this study, an accumulation of H_2O_2 can also be responsible for inhibiting the activity of GOx here. Also, the Michaelis–Menten constants K_M for the catalysts LPMS-50-50T + GOx and LPMS-50-75T + GOx have lower affinities for the substrate glucose as compared to free GOx or to the co-immobilized GOx with HRP on the same materials (Table 5). This points at a higher affinity of GOx to the substrate when present in the vicinity of HRP on the support as opposed to the larger distance in free solution.[66,67]

The maximum rate r_{max} of the free GOx in solution is not comparable to the values reported in the literature ($8.7\ 10^{-3}$–$10.9\ 10^{-3}$ M s^{-1}).[52,53,64] Also, the catalytic reaction rate constant k_{cat} that is independent of the enzyme concentration is lower than the ones reported in the literature (250–310 s^{-1}).[52,53,64] This might be due to an overestimation of the amount of active enzymes caused by denaturation during enzyme preparation. However, the apparent catalytic efficiencies $k_{cat}\ K_M^{-1}$ of the free and the immobilized GOx (7.8–32.0 $mM^{-1}\ s^{-1}$) are in the same range as the values reported in the literature (16.7–88.6 $mM^{-1}\ s^{-1}$).[52,53,64]

The catalytic efficiencies of the catalysts LPMS-50-50T + GOx and LPMS-50-75T + GOx are lower compared to the free GOx despite comparable or higher k_{cat} values. This can be explained by the lower affinities to the glucose substrate of individually immobilized GOx in comparison with free GOx in solution. This is consistent with a higher local concentration of the substrate molecules in the immediate vicinity of the active center of the immobilized *vs.* the free enzyme.

For the catalyst with both GOx and HRP co-immobilized on LPMS-50-50T + GOx/HRP, the k_{cat} value is lower by a factor of 4.5 and also, the catalytic efficiency is slightly lower when compared to the free GOx in solution (Table 5). Interestingly, for the catalyst with the higher fraction of MCM-41-type pores LPMS-50-75T + GOx/HRP, the calculated k_{cat} value (48.7 s^{-1}) and the catalytic efficiency (30.8 $mM^{-1}\ s^{-1}$) are both comparable to the ones of the free GOx. It can, thus, be assumed that the higher fractions of the smaller MCM-41-type pores and the high interconnectivity in the support allow for a closer intimacy and more efficient cooperation between the HRP and GOx enzymes as compared to the ones with GOx individually immobilized with HRP in free solution.

Particle size effect

The influence of the particle size of the hierarchical LPMS materials on the normalized activities of co-immobilized GOx and HRP enzymes was studied by replicating the experiment 3 times for each support. Thus, LPMS-*x*-*y*T materials with maximum particle sizes of 50, 125, and 250 μm were used. As for the previous studies, the loading of GOx and HRP on the supports was the same as that used for the activity studies reported above (*cf.* Table 5) with a HRP : GOx mass ratio of 1 : 3 (see the SI, section S4 and Table S2).

Remarkably, for both supports with the lower (LPMS-*x*-50T) and higher (LPMS-*x*-75T) fractions of the MCM-41-type mesopores, the immobilized enzyme conjugate with the largest particles of 250 μm has the highest normalized activity, even considerably higher than that of the free

Table 5 Apparent Michaelis–Menten constant K_M, maximum reaction rate r_{max}, catalytic reaction rate constant k_{cat}, and catalytic efficiency $k_{cat}\ K_M^{-1}$ of free GOx and of GOx immobilized on large-pore mesoporous silica LPMS-50-*y*T materials with HRP either in solution or co-immobilized

Catalyst	K_M mM^{-1}	$r_{max}/10^{-6}$ M s^{-1}	k_{cat}/s^{-1}	$k_{cat}\ K_M^{-1}/mM^{-1}\ s^{-1}$
Free GOx	1.45	10.28	46.3	32.0
LPMS-50-50T + GOx	2.51	11.88	42.8	17.1
LPMS-50-75T + GOx	8.20	14.26	64.3	7.8
LPMS-50-50T + GOx/HRP	0.39	1.33	10.3	26.3
LPMS-50-75T + GOx/HRP	1.58	1.44	48.7	30.8

enzymes in solution (131 ± 5% and 143 ± 8% for LPMS-250-50T and LPMS-250-75T, Fig. 15). Moreover, the normalized activity decreases with the particle size (82 ± 3% and 67 ± 1% for LPMS-125-50T and LPMS-50-50T and 103 ± 3% and 76 ± 2% for LPMS-125-75T and LPMS-50-75T, respectively, Fig. 15). This can be seen as an indication that the rate of the cascade reaction is likely not limited by diffusion within the monolithic particles. A first explanation for the higher normalized activity with larger support particles is that the enzyme conjugates, at comparable loading, could be more distributed throughout the particles, offering a more favorable spatial arrangement. Therefore, the enzyme conjugates could be more accessible in supports with larger particles compared to those with smaller particles.[68] It cannot be excluded, however, that enzymes might be closer to each other even in the larger particles leading to favorable microenvironments and higher normalized activities.[69]

Note also that, again, the normalized activity for the support with the higher fraction of the MCM-41-type mesopores is higher (*cf.* Table 5). This corroborates the above-mentioned conclusion that the smaller mesopores support the interaction between the two enzymes by efficiently placing the enzymes in close proximity. This is also consistent with the interconnectivity of the two mesopore systems as derived from the PFG NMR showing decreased diffusion coefficients for these materials with higher fractions of MCM-41 pores (*cf.* Table 4). It might, therefore, be conceived that the higher activity in the catalysts with more smaller mesopores (and with larger particles) is related to the higher residence time of the substrates and intermediates in the vicinity of the active sites of the enzymes located within the pore system of the supports.[55,70]

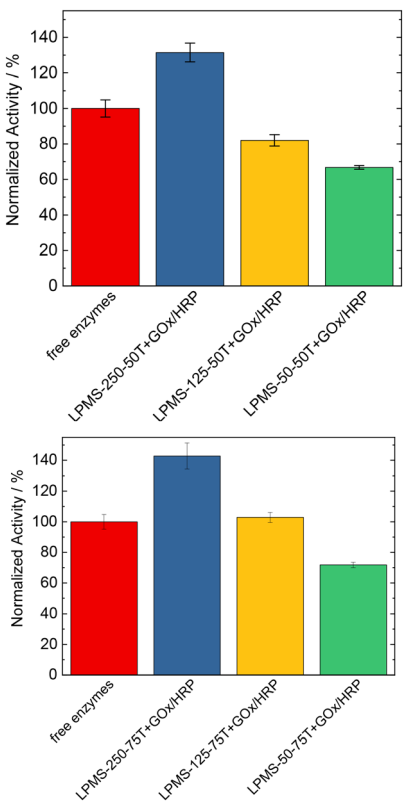

Fig. 15 Normalized activity of the free and of the co-immobilized GOx and HRP on large-pore mesoporous silica with different particle sizes and different MCM-41 pore fractions LPMS-*x*-50T (top) and LPMS-*x*-75T (bottom).

Stability of the biocatalysts

In a first set of the experiments, the temperature influence on the activity of the multi-enzyme conjugate immobilized on the hierarchical large-pore mesoporous silica with different particle sizes LPMS-*x*-75T was studied in the range of 288 to 328 K. As expected, the normalized activity increases with the reaction temperature, however only up to 318 K, where the highest activity for both free enzymes and supported enzymes was observed (see the SI, section S6.1 and Fig. S11). These results are in agreement with the ones reported in the literature, as it was shown that GOx is stable up to 323 K (ref. 63) and HRP up to 328 K.[71] Consequently, the activity at 328 K is much lower than that at 318 K due to denaturation of the enzymes. In addition, the normalized activity as well as its increase with temperature is more pronounced for the support with larger particles than that for the support with smaller particles (SI, Fig. S11). Although this might be taken as an indication for the reduced role of diffusion limitations (for which the activity increase with temperature is expected to be comparable), these results do not allow to draw a final conclusion regarding a diffusion limitation of the reaction as a higher temperature increases both reaction and diffusion rates.

Moreover, the influence of storage temperature between 278 and 353 K for 4 h and the effect of storage time up to 16 days at 278 K on the enzymes GOx and HRP co-immobilized on the LPMS-*x*-75T materials was investigated (see the SI, sections S6.2 and S6.3). Generally, the enzymes are relatively stable when stored for 4 h up to 318 K, whereas the relative activity drops due to denaturation at higher temperatures. Storage over extended duration at 278 K leads to a steady decrease in relative activity. This activity decrease is less pronounced for the material with 250 μm particle size than for that with smaller particles, which supports the above-mentioned conclusion that the enzymes in the larger particles are located within the pores of the monolithic particles and are, thus, more efficiently protected from leaching.

Conclusions

In conclusion, monolithic large-pore mesoporous silica (LPMS) with a hierarchical system of two interconnected mesopore systems of ordered MCM-41-type pores (2.4–5.5 nm) and unordered LPMS-type mesopores (20–40 nm) was prepared *via* partial pseudomorphic transformation. The homogeneous distribution and interconnectivity of the two mesopore systems were verified by HR-TEM and PFG NMR.

These materials were successfully applied to co-immobilize GOx and HRP as two enzymes with different sizes, proposing a spatial arrangement targeting the two differently sized mesopore systems. These co-immobilized enzymes are more active than the free enzymes in solution when supported on hierarchical LPMS monoliths with particles sizes above 125 μm. Challenges remain in improving the stability of the enzymes, especially against leaching upon reuse by either milder washing, crosslinking, or surface functionalization of the silica material. Clearly, this approach can be extended to support other enzyme conjugates by adapting the width (distribution) and the relative fraction of the mesopore systems. The monolithic nature of the multi-enzyme conjugate-based biocatalysts makes them attractive and promising candidates for future continuous-flow processing for advanced and sustainable biotechnological transformations. Introducing even more complex pore architectures for immobilizing more than two types of cooperating enzymes might eventually pave the way for rationally designing artificial cells.

Author contributions

Georgia Mhanna: conceptualization, methodology, investigation, data curation, writing – original draft. Muslim Dvoyashkin: investigation, data curation. David Poppitz: investigation, data curation, writing – review & editing. Roger Gläser: funding acquisition, resources, supervision, writing – review & editing.

Conflicts of interest

There are no conflicts to declare.

Data availability

The supporting data have been provided as part of the supplementary information (SI). It consists of 11 pages, 6 sections, 15 figures, 3 tables and 2 references. It contains information on preparation of alkyltrimethylammonium hydroxide solutions, on characterization of partially transformed large-pore mesoporous silica materials (LPMS-*x*-*y*T), on preparation of mesocellular foam, on enzyme immobilization, on enzyme activity and enzyme kinetics and stablity of the immobilized enzymes.

Supplementary information is available. See DOI: https://doi.org/10.1039/d5cy01546d.

Acknowledgements

Georgia Mhanna acknowledges the support through the German Academic Exchange Service (DAAD) for the Graduate School Scholarship Programme (Programm zur Förderung ausländischer Doktorandinnen und Doktoranden in strukturierten Promotionsprogrammen) 2014-57034101. The authors thank Prof. W.-D. Einicke, Institute of Chemical Technology, Universität Leipzig, Germany, for his support in investigation and data curation on pseudomorphic transformation and nitrogen sorption. Thanks are also due to Prof. Dr. S. Ebbinghaus, Institut für Chemie, Martin-Luther-Universität Halle-Wittenberg, Germany, for providing XRD data on selected materials.

References

1 J. Fu, M. Liu, Y. Liu, N. W. Woodbury and H. Yan, Interenzyme Substrate Diffusion for an Enzyme Cascade Organized on Spatially Addressable DNA Nanostructures, *J. Am. Chem. Soc.*, 2012, **134**, 5516–5519.
2 J. C. Reisenbauer, K. M. Sicinski and F. H. Arnold, Catalyzing the future: recent advances in chemical synthesis using enzymes, *Curr. Opin. Chem. Biol.*, 2024, **83**, 102536.
3 U. T. Bornscheuer, (Chemo-) enzymatic cascade reactions, *Z. Naturforsch., C: J. Biosci.*, 2019, **74**, 61–62.
4 S. Wang, L. Wang, X. Yan and B. Jiang, Cascade Catalytic Nanozymes: Design, Classification, and Biomedical Applications, *ACS Appl. Mater. Interfaces*, 2025, **17**, 45354–45381.
5 A. Kuchler, M. Yoshimoto, S. Luginbuhl, F. Mavelli and P. Walde, Enzymatic reactions in confined environments, *Nat. Nanotechnol.*, 2016, **11**, 409–420.
6 E. Ricca, B. Brucher and J. H. Schrittwieser, Multi-Enzymatic Cascade Reactions: Overview and Perspectives, *Adv. Synth. Catal.*, 2011, **353**, 2239–2262.
7 W. Liu, S. Zhang and P. Wang, Nanoparticle-supported multi-enzyme biocatalysis with in situ cofactor regeneration, *J. Biotechnol.*, 2009, **139**, 102–107.
8 M. Zheng, S. Zhang, G. Ma and P. Wang, Effect of molecular mobility on coupled enzymatic reactions involving cofactor regeneration using nanoparticle-attached enzymes, *J. Biotechnol.*, 2011, **154**, 274–280.
9 S. Kwon, M. P. Andreas and T. W. Giessen, Pore Engineering as a General Strategy to Improve Protein-Based Enzyme Nanoreactor Performance, *ACS Nano*, 2024, **18**, 25740–25753.
10 T. Chen, Y. Lu, X. Xiong and Z. Xu, Co-immobilization of enzymes and chemocatalysts for one-pot chemoenzymatic cascades: Scaffold engineering toward more efficient catalysis, *Chem Catal.*, 2024, **4**, 100894.
11 K. Xu, X. Chen, R. Zheng and Y. Zheng, Immobilization of Multi-Enzymes on Support Materials for Efficient Biocatalysis, *Front. Bioeng. Biotechnol.*, 2020, **8**, 660.
12 N. Balistreri, D. Gaboriau, C. Jolivalt and F. Launay, Covalent immobilization of glucose oxidase on mesocellular silica foams: Characterization and stability towards temperature and organic solvents, *J. Mol. Catal. B: Enzym.*, 2016, **127**, 26–33.
13 D. Gaffney, N. H. Abdallah, J. C. Cooney, F. R. Laffir, K. E. Cassimjee, P. Berglund, U. Hanefeld and E. Magner, Preparation and characterisation of a Ni^{2+}/Co^{2+}-cyclam modified mesoporous cellular foam for the specific immobilisation of His6-alanine racemase, *J. Mol. Catal. B: Enzym.*, 2014, **109**, 154–160.
14 N. Carlsson, H. Gustafsson, C. Thörn, L. Olsson, K. Holmberg and B. Åkerman, Enzymes immobilized in mesoporous silica: a physical-chemical perspective, *Adv. Colloid Interface Sci.*, 2014, **205**, 339–360.

15 J. Zhang, J. F. Lovell, J. Shi and Y. Zhang, Nanomaterials for co-immobilization of multiple enzymes, *BMEMat*, 2025, **3**, e12080.
16 Y. Han, S. S. Lee and J. Y. Ying, Pressure-Driven Enzyme Entrapment in Siliceous Mesocellular Foam, *Chem. Mater.*, 2006, **18**, 643–649.
17 B. Karimi, S. Emadi, A. A. Safari and M. Kermanian, Immobilization, stability and enzymatic activity of albumin and trypsin adsorbed onto nanostructured mesoporous SBA-15 with compatible pore sizes, *RSC Adv.*, 2014, **4**, 4387–4394.
18 F. Jia, B. Narasimhan and S. Mallapragada, Materials-based strategies for multi-enzyme immobilization and co-localization: A review, *Biotechnol. Bioeng.*, 2014, **111**, 209–222.
19 M. Hartmann and X. Kostrov, Immobilization of enzymes on porous silicas–benefits and challenges, *Chem. Soc. Rev.*, 2013, **42**, 6277–6289.
20 Z. Zhou and M. Hartmann, Progress in enzyme immobilization in ordered mesoporous materials and related applications, *Chem. Soc. Rev.*, 2013, **42**, 3894–3912.
21 E. Magner, Immobilisation of enzymes on mesoporous silicate materials, *Chem. Soc. Rev.*, 2013, **42**, 6213–6222.
22 M. Dreifke, F. J. Brieler and M. Froeba, Immobilization of Alcohol Dehydrogenase from E-coli onto Mesoporous Silica for Application as a Cofactor Recycling System, *ChemCatChem*, 2017, **9**, 1197–1210.
23 M. Dreifke, D. I. Fried, F. J. Brieler and M. Froeba, Kinetic investigations of 6-phosphogluconate dehydrogenase confined in mesoporous silica, *J. Mol. Catal. B: Enzym.*, 2016, **132**, 5–15.
24 J. Fan, J. Lei, L. Wang, C. Yu, B. Tu and D. Zhao, Rapid and high-capacity immobilization of enzymes based on mesoporous silicas with controlled morphologies, *Chem. Commun.*, 2003, 2140.
25 P. Jain, A. K. Minhas, P. Kaur, P. K. Manna, M. Puri, C. J. Barrow and S. Mandal, Silica nanobiocatalyst: Advancements toward sustainable and innovative applications, *Next Nanotechnol.*, 2024, **6**, 100068.
26 H. Yang, Y. Lin, Q. Mo, Z. Li, F. Yang and X. Li, Monitoring Enzymatic Reaction Kinetics and Activity Assays in Confined Nanospace, *Anal. Chem.*, 2024, **96**(30), 12404–12413.
27 S. Majeed, R. Nawaz, T. Rasheed and M. Bilal, in *Nanomaterials for Biocatalysis*, ed. G. R. Castro, Elsevier, San Diego, 2021, pp. 171–188.
28 A. Costantini, V. Venezia, G. Pota, A. Bifulco, V. Califano and F. Sannino, Adsorption of Cellulase on Wrinkled Silica Nanoparticles with Enhanced Inter-Wrinkle Distance, *Nanomaterials*, 2020, **10**(9), 1799.
29 G. Pota, A. Bifulco, D. Parida, S. Zhao, D. Rentsch, E. Amendola, V. Califano and A. Costantini, Tailoring the hydrophobicity of wrinkled silica nanoparticles and of the adsorption medium as a strategy for immobilizing lipase: An efficient catalyst for biofuel production, *Microporous Mesoporous Mater.*, 2021, **328**, 111504.
30 N. H. Abdallah, M. Schlumpberger, D. A. Gaffney, J. P. Hanrahan, J. M. Tobin and E. Magner, Comparison of mesoporous silicate supports for the immobilisation and activity of cytochrome c and lipase, *J. Mol. Catal. B: Enzym.*, 2014, **108**, 82–88.
31 M. Piras, A. Salis, M. Piludu, D. Steri and M. Monduzzi, 3D vision of human lysozyme adsorbed onto a SBA-15 nanostructured matrix, *Chem. Commun.*, 2011, **47**, 7338–7340.
32 P. H. Pandya, R. V. Jasra, B. L. Newalkar and P. N. Bhatt, Studies on the activity and stability of immobilized α-amylase in ordered mesoporous silicas, *Microporous Mesoporous Mater.*, 2005, **77**, 67–77.
33 E. Weber, D. Sirim, T. Schreiber, B. Thomas, J. Pleiss, M. Hunger, R. Gläser and V. B. Urlacher, Immobilization of P450 BM-3 monooxygenase on mesoporous molecular sieves with different pore diameters, *J. Mol. Catal. B: Enzym.*, 2010, **64**, 29–37.
34 N. Ž. Knežević and J.-O. Durand, Large pore mesoporous silica nanomaterials for application in delivery of biomolecules, *Nanoscale*, 2015, **7**, 2199–2209.
35 T. Martin, A. Galarneau, F. Di Renzo, F. Fajula and D. Plee, Morphological Control of MCM-41 by Pseudomorphic Synthesis, *Angew. Chem., Int. Ed.*, 2002, **41**, 2590–2592.
36 W.-D. Einicke, H. Uhlig, D. Enke, R. Gläser, C. Reichenbach and S. G. Ebbinghaus, Synthesis of hierarchical micro/mesoporous Y-zeolites by pseudomorphic transformation, *Colloids Surf., A*, 2013, **437**, 108–112.
37 A. Inayat, B. Reinhardt, H. Uhlig, W.-D. Einicke and D. Enke, Silica monoliths with hierarchical porosity obtained from porous glasses, *Chem. Soc. Rev.*, 2013, **42**, 3753–3764.
38 A. Galarneau, F. Villemot, J. Rodriguez, F. Fajula and B. Coasne, Validity of the t-plot method to assess microporosity in hierarchical micro/mesoporous materials, *Langmuir*, 2014, **30**, 13266–13274.
39 W.-D. Einicke, D. Enke, M. Dvoyashkin, R. Valiullin and R. Gläser, The Mechanism of Pseudomorphic Transformation of Spherical Silica Gel into MCM-41 Studied by PFG NMR Diffusometry, *Materials*, 2013, **6**, 3688–3709.
40 E. Moreno-Reyes and J. M. Goddard, Hierarchical materials: An overview of synthesis methods and revolutionary impact on enzyme biocatalysis, *Colloids Surf., B*, 2025, **256**, 115086.
41 A. Galarneau, J. Iapichella, K. Bonhomme, F. Di Renzo, P. Kooyman, O. Terasaki and F. Fajula, Controlling the morphology of mesostructured silicas by pseudomorphic transformation: A route towards applications, *Adv. Funct. Mater.*, 2006, **16**, 1657–1667.
42 J. Garcia-Martinez, K. Li and M. E. Davis, *Mesoporous zeolites. Preparation, characterization and applications*, Wiley-VCH, Weinheim, Germany, 2015.
43 H. Uhlig, T. Muenster, G. Kloess, S. G. Ebbinghaus, W.-D. Einicke, R. Gläser and D. Enke, Synthesis of MCM-48 granules with bimodal pore systems via pseudomorphic transformation of porous glass, *Microporous Mesoporous Mater.*, 2018, **257**, 185–192.
44 A. Hart and J. Wood, Methodological review of zeolite synthesis from industrial waste and natural clays and the fabrication of hierarchical pore structures, *Next Mater.*, 2025, **9**, 101113.

45 D. Rando, G. W. Kohring and F. Giffhorn, Production, purification and characterization of glucose oxidase from a newly isolated strain of Penicillium pinophilum, *Appl. Microbiol. Biotechnol.*, 1997, **48**, 34–40.

46 D. Feng, T.-F. Liu, J. Su, M. Bosch, Z. Wei, W. Wan, D. Yuan, Y.-P. Chen, X. Wang, K. Wang, X. Lian, Z.-Y. Gu, J. Park, X. Zou and H.-C. Zhou, Stable metal-organic frameworks containing single-molecule traps for enzyme encapsulation, *Nat. Commun.*, 2015, **6**, 1–8.

47 P. Feng, X. Bu and D. J. Pine, Control of Pore Sizes in Mesoporous Silica Templated by Liquid Crystals in Block Copolymer–Cosurfactant–Water Systems, *Langmuir*, 2000, **16**, 5304–5310.

48 D. Chen, Z. Li, Y. Wan, X. Tu, Y. Shi, Z. Chen, W. Shen, C. Yu, B. Tu and D. Zhao, Anionic surfactant induced mesophase transformation to synthesize highly ordered large-pore mesoporous silica structures, *J. Mater. Chem.*, 2006, **16**, 1511.

49 P. I. Ravikovitch, G. L. Haller and A. V. Neimark, Density functional theory model for calculating pore size distributions: pore structure of nanoporous catalysts, *Adv. Colloid Interface Sci.*, 1998, **76**, 203–226.

50 in *Annual Reports on NMR Spectroscopy*, ed. J. Farjon, L. Ziani, L. Beguin, D. Merlet, J. Courtieu and G. A. Webb, Elsevier, 2007, vol. 61.

51 A. Galarneau, F. Guenneau, A. Gedeon, D. Mereib, J. Rodriguez, F. Fajula and B. Coasne, Probing Interconnectivity in Hierarchical Microporous/Mesoporous Materials Using Adsorption and Nuclear Magnetic Resonance Diffusion, *J. Phys. Chem. C*, 2016, **120**, 1562–1569.

52 X. Cao, Y. Li, Z. Zhang, J. Yu, J. Qian and S. Liu, Catalytic activity and stability of glucose oxidase/horseradish peroxidase co-confined in macroporous silica foam, *Analyst*, 2012, **137**, 5785–5791.

53 P. Pescador, I. Katakis, J. L. Toca-Herrera and E. Donath, Efficiency of a bienzyme sequential reaction system immobilized on polyelectrolyte multilayer-coated colloids, *Langmuir*, 2008, **24**, 14108–14114.

54 A. Curulli, A. Cusma, S. Kaciulis, G. Padeletti, L. Pandolfi, F. Valentini and M. Viticoli, Immobilization of GOD and HRP enzymes on nanostructured substrates, *Surf. Interface Anal.*, 2006, **38**, 478–481.

55 D. Mackey, A. J. Killard, A. Ambrosi and M. R. Smyth, Optimizing the ratio of horseradish peroxidase and glucose oxidase on a bienzyme electrode, *Sens. Actuators, B*, 2007, **122**, 395–402.

56 H. Liang, S. Jiang, Q. Yuan, G. Li, F. Wang, Z. Zhang and J. Liu, Co-immobilization of multiple enzymes by metal coordinated nucleotide hydrogel nanofibers: improved stability and an enzyme cascade for glucose detection, *Nanoscale*, 2016, **8**, 6071–6078.

57 S. Vasenkov and J. Karger, Long-range diffusion in beds of nanoporous particles: pitfalls and potentials, *Magn. Reson. Imaging*, 2005, **23**, 139–145.

58 Z. Adem, F. Guenneau, M.-A. Springuel-Huet, A. Gédéon, J. Iapichella, T. Cacciaguerra and A. Galarneau, Diffusion Properties of Hexane in Pseudomorphic MCM-41 Mesoporous Silicas Explored by Pulsed Field Gradient NMR, *J. Phys. Chem. C*, 2012, **116**, 13749–13759.

59 S. Hudson, J. Cooney and E. Magner, Proteins in mesoporous silicates, *Angew. Chem., Int. Ed.*, 2008, **47**, 8582–8594.

60 A. Y. Khan, S. B. Noronha and R. Bandyopadhyaya, Impact of structural features of SBA-15 host particles on activity of immobilized glucose oxidase enzyme and sensitivity of a glucose sensor, *J. Porous Mater.*, 2015, **22**, 369–378.

61 W. Chouyyok, J. Panpranot, C. Thanachayanant and S. Prichanont, Effects of pH and pore characters of mesoporous silicas on horseradish peroxidase immobilization, *J. Mol. Catal. B: Enzym.*, 2009, **56**, 246–252.

62 S. Gao, Y. Wang, X. Diao, G. Luo and Y. Dai, Effect of pore diameter and cross-linking method on the immobilization efficiency of Candida rugosa lipase in SBA-15, *Bioresour. Technol.*, 2010, **101**, 3830–3837.

63 C. M. Wong, K. H. Wong and X. D. Chen, Glucose oxidase: natural occurrence, function, properties and industrial applications, *Appl. Microbiol. Biotechnol.*, 2008, **78**, 927–938.

64 Y. Zhang, S. Tsitkov and H. Hess, Proximity does not contribute to activity enhancement in the glucose oxidase-horseradish peroxidase cascade, *Nat. Commun.*, 2016, **7**, 13982.

65 J. M. Harris, C. Reyes and G. P. Lopez, Common causes of glucose oxidase instability in in vivo biosensing: a brief review, *J. Diabetes Sci. Technol.*, 2013, **7**, 1030–1038.

66 S. Barricella, J. M. Fuertes, K. H. Putera, A. E. Quigley, V. Haritos, B. D. Freeman and G. Garnier, Spatially confined enzymatic tandem system with GOx and HRP compartmentalized in ultrafiltration membrane, *J. Membr. Sci.*, 2024, **690**, 122214.

67 R. Ahmad, J. Shanahan, S. Rizaldo, D. S. Kissel and K. L. Stone, Co-immobilization of an Enzyme System on a Metal-Organic Framework to Produce a More Effective Biocatalyst, *Catalysts*, 2020, **10**, 499.

68 I.-A. Pavel, S. F. Prazeres, G. Montalvo, C. Garcı A Ruiz, V. Nicolas, A. Celzard, F. Dehez, L. Canabady-Rochelle, N. Canilho and A. Pasc, Effect of Meso vs Macro Size of Hierarchical Porous Silica on the Adsorption and Activity of Immobilized β-Galactosidase, *Langmuir*, 2017, **33**, 3333–3340.

69 J. Muschiol, C. Peters, N. Oberleitner, M. D. Mihovilovic, U. T. Bornscheuer and F. Rudroff, Cascade catalysis - strategies and challenges en route to preparative synthetic biology, *Chem. Commun.*, 2015, **51**, 5798–5811.

70 E. R. Stadtman and P. B. Chock, *From metabolite, to metabolism, to metabolon*, Academic Press, San Diego, 1992.

71 Q. Lu, Y. Kim, N. Bassim, N. Raman and G. E. Collins, Catalytic activity and thermal stability of horseradish peroxidase encapsulated in self-assembled organic nanotubes, *Analyst*, 2016, **141**, 2191–2198.